THE ASTROPHYSICAL JOURNAL, 438:120–134, 1995 January 1

MULTIWAVELENGTH MONITORING OF THE BL LACERTAE OBJECT PKS 2155−304. IV. MULTIWAVELENGTH ANALYSIS

R. EDELSON,[1,2] J. KROLIK,[3] G. MADEJSKI,[1] L. MARASCHI,[4] G. PIKE,[1] C. M. URRY,[5] W. BRINKMANN,[6] T. J.-L. COURVOISIER,[7] J. ELLITHORPE,[8] K. HORNE,[9] A. TREVES,[10] S. WAGNER,[11] W. WAMSTEKER,[12] R. WARWICK,[13] H. D. ALLER,[14] M. F. ALLER,[14] M. ASHLEY,[15] A. BLECHA,[7] P. BOUCHET,[16] P. BRATSCHI,[7] J. N. BREGMAN,[14] M. CARINI,[17] A. CELOTTI,[18] M. DONAHUE,[19] E. FEIGELSON,[20] A. V. FILIPPENKO,[21] H. FINK,[6] I. GEORGE,[1] I. GLASS,[22] J. HEIDT,[11] J. HEWITT,[8] P. HUGHES,[14] R. KOLLGAARD,[20] Y. KONDO,[23] A. KORATKAR,[5] K. LEIGHLY,[1] A. MARSCHER,[24] P. G. MARTIN,[25] T. MATHESON,[21] H. R. MILLER,[26] J. C. NOBLE,[26] P. O'BRIEN,[27] E. PIAN,[10] G. REICHERT,[1] J. M. SAKEN,[5,28] J. M. SHULL,[28] M. SITKO,[29] P. S. SMITH,[30] W.-H. SUN,[31] AND G. TAGLIAFERRI[32]

Received 1993 August 13; accepted 1994 July 13

ABSTRACT

Simultaneous X-ray, ultraviolet, optical, infrared, and radio monitoring data were used to test and constrain models of continuum emission from the BL Lacertae object PKS 2155−304. Intensively sampled ultraviolet and soft X-ray light curves showed a clear temporal correlation, with the X-rays leading the ultraviolet by 2–3 hr. This lag was found to be significantly different from zero after an exhaustive comparison of four different techniques for measuring temporal correlations. Variations in the ultraviolet through optical wave bands were also all strongly correlated, with no measurable lag down to limiting timescales of $\lesssim$1–2 hr. This strong correlation extends to the near-infrared, but the less intensive sampling precludes measurement of any lag beyond an upper limit of $\lesssim$1 day. These lags and limits of the order of hours are much shorter than the most rapid observed single-band variations. Because of the very sparse radio sampling, it was not possible to measure quantitatively the correlation and lag with shorter wavelengths, but the data do suggest that the radio may lag the optical/ultraviolet by $\sim$1 week, with longer delays and weaker variations to longer radio wavelengths. The epoch-folding Q^2 statistic was used to test for periodicity, and no evidence for strict or quasi-periodicity was found in any of the light curves.

Because they lead the lower frequencies, the soft X-rays ($\lesssim$1 keV) cannot arise from synchrotron self-Compton scattering. These results also rule out the accretion disk model, which predicts a measurable lag between ultraviolet/optical wavelength bands and a correlation between hardness and brightness, neither of which were seen. They are consistent with the entire radio through X-ray continuum arising from direct synchrotron emission from a relativistic jet. However, the tapered jet model, in which the X-ray emission is produced closer in, has problems explaining the magnitude of the ultraviolet/X-ray lag, because the

[1] Laboratory for High Energy Astrophysics, Code 666, NASA/GSFC, Greenbelt, MD 20771.
[2] Department of Physics and Astronomy, University of Iowa City, IA 52242.
[3] Johns Hopkins University, Department of Physics and Astronomy, Baltimore, MD 21218.
[4] Department of Physics, University of Milan, via Celoria 16, I-20133 Milan, Italy.
[5] Space Telescope Science Institute, 3700 San Martin Drive, Baltimore, MD 21218.
[6] Max-Planck-Institut für Extraterrestrische Physik, Giessenbachstrasse, D-8046 Garching bei München, Germany.
[7] Observatoire de Genève, chemin des Maillettes 51, CH-1290 Sauverny, Switzerland.
[8] Department of Physics, Massachusetts Institute of Technology, Cambridge, MA 02139.
[9] Sterrekundig Instituut Utrecht, Postbus 80000, 3508TA Utrecht, the Netherlands.
[10] SISSA International School of Advanced Studies, Trieste, Italy.
[11] Landessternwarte Heidelberg-Königstuhl, Königstuhl, D-69117 Heidelberg, Germany.
[12] ESA *IUE* Observatory, P.O. Box 50727, 28080 Madrid, Spain.
[13] Department of Physics, University of Leicester, University Road, Leicester LE1 7RH, England.
[14] Department of Astronomy, Dennison Building, University of Michigan, Ann Arbor, MI 48109-1090.
[15] Department of Astronomy, University of New South Wales, Kensington, NSW 2033, Australia.
[16] European Southern Observatory, Casilla 19001, Santiago 19, Chile.
[17] Computer Sciences Corporation, NASA/GSFC, Greenbelt, MD 20771.
[18] Institute of Astronomy, Cambridge University, Madingley Road, Cambridge CB3 0HA, UK.
[19] Carnegie Observatories, 813 Santa Barbara Street, Pasadena, CA 91101.
[20] Department of Astronomy and Astrophysics, 525 Davey Lab, Pennsylvania State University, University Park, PA 16802.
[21] Department of Astronomy, University of California, Berkeley, Berkeley CA 94720.
[22] South Africa Astronomical Observatory, P.O. Box 9, Observatory 7935, South Africa.
[23] Laboratory for Astronomy and Solar Physics, Code 684, NASA/GSFC, Greenbelt, MD 20771.
[24] Department of Astronomy, Boston University, 725 Commonwealth Avenue, Boston, MA 02215-1401.
[25] Canadian Institute for Theoretical Astrophysics, University of Toronto, Toronto, ON, Canada M5S 1A1.
[26] Department of Physics, Georgia State University, Atlanta, GA 30303.
[27] Department of Astrophysics, Nuclear Physics Laboratory, Keble Road, Oxford OX1 3RH, UK.
[28] Center for Astrophysics and Space Astronomy, CB 389, University of Colorado, Boulder, CO 80302-0389.
[29] Department of Physics, University of Cincinnati, Cincinnati, OH 45221-0011.
[30] Steward Observatory, University of Arizona, Tucson, AZ 85721.
[31] National Central University, Institute of Astronomy, 32054 Chung-Li, ROC, Taiwan.
[32] Osservatorio Astronomico di Brera, via Brera 28, I-20121 Milan, Italy.

X-ray–emitting electrons have very short lifetimes ($t_{1/2} \ll 1$ s). The result that the lag is much smaller than the variability timescale suggests instead that the radiation may be produced in a flattened region such as a shock front.

Subject headings: BL Lacertae objects: individual (PKS 2155−304) — galaxies: active — infrared: galaxies — radio continuum: galaxies — ultraviolet: galaxies — X-rays: galaxies

1. INTRODUCTION

Determining the physical process(es) responsible for the large ($L \gtrsim 10^{12}\ L_\odot$) luminosities has always been one of the central problems in research on active galactic nuclei (AGN). The continuum emission is thought to arise closer to the center than the line emission, and since BL Lacertae objects are the AGN for which the continuum is most dominant, their behavior may yield clues about the physical conditions nearest the center. Unlike the less active AGN (normal quasars and Seyfert galaxies), BL Lac objects have highly polarized ($p \gtrsim 5\%$) optical/infrared continua, which are generally devoid of strong, broad emission lines. Their smooth radio through ultraviolet spectral energy distributions (SEDs) are generally well described as a single parabolic component, although the X-rays often lie above a simple extrapolation from lower energies. This suggests that with BL Lac objects we may be seeing as close as possible to the central engine, without complications such as emission or obscuration from surrounding regions. This interpretation is supported by the observation of rapid variations at many wavelengths (e.g., Quirrenbach et al. 1991; Edelson 1992), indicative of emission directly from a very compact region and/or relativistic enhancement.

Strong multiwavelength variability provides several important clues to the identity of the mechanism responsible for the continuum emission from BL Lac objects. Early studies showed that some radio sources varied so rapidly that if the emission were isotropic, the "Compton catastrophe" would lead to much larger X-ray fluxes than were actually observed (e.g., Marscher et al. 1979). The most widely accepted explanation advanced to date is that the emission is direct synchrotron radiation from a jet of high-energy electrons moving toward us with highly relativistic bulk velocities (see, e.g., the review by Bregman 1990). These conclusions were reinforced by observations of superluminal motion (e.g., Cohen & Unwin 1981), in which emission components appear to separate at speeds well in excess of the speed of light. This "beaming" model was given further support by X-ray observations, which, in at least a few cases, found variations that were too rapid to be consistent with limits on $\Delta L/\Delta t$ derived assuming isotropic emission.

However, in its simplest version, which postulates a homogeneous region and a power-law energy spectrum for the electrons [$N(E) \propto E^{-s}$], the above process cannot explain the full SEDs of BL Lac objects, which show an overall downward curvature when νF_ν is plotted as a function of ν (see Fig. 1). Either multiple components, an inhomogeneous or nonaxisymmetric region, or non–power-law particle spectra are required (e.g., Königl 1989). The success of these modified models in reproducing the radio through ultraviolet SEDs may be due in part to the fact that there are a number of free parameters and assumptions built in (e.g., the shape of the jet and the variation of the physical parameters along it; see Ghisellini, Maraschi, & Treves 1985). Synchrotron emission may extend into the X-ray band, at least in some objects, while the Compton process could be expected to produce a flat X-ray/γ-ray component. Because PKS 2155−304 has a steep X-ray spectrum (e.g., Treves et al. 1989), it has been argued that synchrotron emission dominates the X-ray emission from this particular object (Urry & Mushotzky 1982; Ghisellini et al. 1985).

Finally, alternatives to the relativistic jet model have been advanced. For instance, it has been proposed that microlensing of quasars by intervening galaxies could explain the high apparent luminosities and lack of line emission (Ostriker & Vietri 1985, 1990). It has also been suggested that the optical/ultraviolet emission could be thermal radiation from an accretion flow (Wandel & Urry 1991).

Multiwavelength variability can resolve many of these issues and allow strong constraints and tests of these models. For example, Compton upscattering of synchrotron photons on relativistic electrons in the same region could not vary more rapidly than or lead the direct synchrotron emission (e.g., Maraschi 1992). Likewise, in the accretion disk model, the lower temperature (lower frequency) radiation comes from farther out in the disk, so the ultraviolet variations should be much stronger and lead those at optical wavelengths.

Previous studies have tried to investigate whether the broadband SEDs evolve in a consistent and reasonable fashion (e.g., George, Warwick, & Bromage 1988; Treves et al. 1989; Mufson et al. 1990). Unfortunately, their temporal sampling and multiwavelength coordination were insufficient to allow determination of the temporal correlations and lags between the bands. Therefore, a large consortium of observers worked together to monitor intensively the BL Lac object PKS 2155−304 during the month of 1991 November.

The observations are discussed in the next section, and a detailed time-series analysis is given in § 3. The implications of these results for the various models of continuum generation in BL Lac objects are presented in § 4, and the results are summarized in § 5.

2. MULTIWAVELENGTH OBSERVATIONS OF PKS 2155−304

PKS 2155−304 was chosen for this intensive multiwavelength monitoring campaign because it is one of the brightest BL Lac objects in the sky at X-ray through optical wavelengths, and has a history of strong, rapid multiwavelength variability (e.g., Edelson et al. 1991: Tagliaferri et al. 1991). Observations were made in 1991 November at X-ray, ultraviolet, optical, near-infrared, and radio wavelengths. Figure 1 shows a time-averaged radio through X-ray SED. The infrared through X-ray data points were derived from observations on November 14.75–15.30, and the radio data were taken on November 16.1. (All dates and times in this paper are in UT.) The SED is very smooth, at least over the wave bands observed in this experiment, rising monotonically in νF_ν from 20 cm (where the mean spectral index is $\langle\alpha\rangle = +0.01$; $S_\nu \propto \nu^\alpha$) to 1400 Å (where $\langle\alpha\rangle = -0.79$). The X-rays (with $\langle\alpha\rangle = -1.65$) show no sign of the flattening that would be expected from Compton scattering.

Typically, each available instrument observed PKS 2155−304 about once per day during the period 1991 November 1–30. Furthermore, an intensive campaign of observations once every 96 minutes was undertaken with *IUE* during the

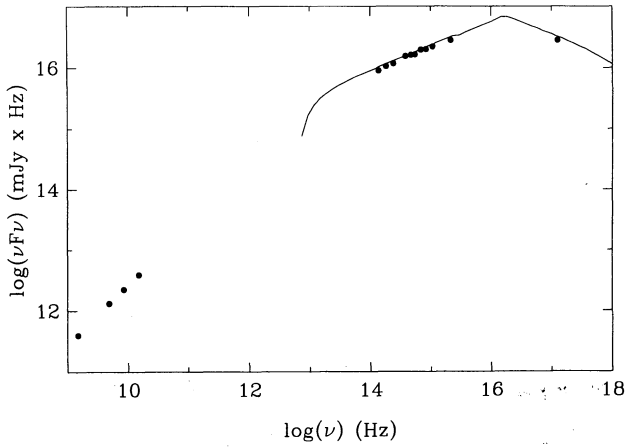

FIG. 1.—SED of PKS 2155−304. This "snapshot" of the broadband spectrum was derived from X-ray through infrared data gathered on November 14.75–15.3 and radio data gathered on November 16.1. The quantity νF_ν is plotted as a function of ν, so a spectral index ($F_\nu \propto \nu^\alpha$) of $\alpha = -1$ (corresponding to equal luminosities per logarithmic frequency interval) is a horizontal line in the plot. Although there are many gaps in the coverage, the SED appears to curve smoothly downward as frequency increases. The solid lines represent the results of fitting a synchrotron model to the data (see text for details).

period November 10.7–15.2, and with *ROSAT* during the period November 12.2–15.3 (excluding time lost to Earth occultations and scheduling problems). The result was the largest and most comprehensive database of multiwavelength observations ever gathered on an AGN in such a short time period. A data set containing over 200 *IUE* spectra, 10^6 *ROSAT* Position Sensitive Proportional Counter (PSPC) photons, and 500 ground-based photometric observations were obtained in this period.

These data are presented in three preceding papers that discuss the data collection and reduction and the single-band analyses. The 25 Å *ROSAT* soft X-ray light curve was taken directly from Brinkmann et al. (1994, hereafter Paper II), and all of the data at $\lambda \geq 3000$ Å were taken directly from Courvoisier et al. (1995, hereafter Paper III). The 1400 Å *IUE* short-wavelength prime (SWP) and 2800 Å *IUE* long-wavelength prime (LWP) data were taken directly from Urry et al. (1993, hereafter Paper I), with the exception that the four 1400 Å points with unusually short integration times ($t_{int} < 30$ minutes, compared with the normal 55 minute exposures) were excluded because of an apparent systematic bias in the calibration (Walter & Courvoisier 1991).

The 5000 Å *IUE* Fine Error Sensor (FES) data were also potentially very useful, but they showed a few large, apparently non-Gaussian excursions, which seriously compromised their value. An unbiased method was devised to improve the data quality so they could be used in time-series analysis. First, the 5000 Å data were paired up, with phases locked to the 96 minute sampling at shorter wavelengths (to aid in correlation analysis). Next, the flux difference (ΔF_i) and averages ($\langle F \rangle_i$) were computed for each (ith) pair. While the data for most pairs were within a few percent, five had $\Delta F_i/\langle F \rangle_i > 10\%$. These five pairs were excluded on the basis of their large internal dispersions. The fractional errors on the remaining 75 points were reduced from 8% (Paper I) to $\lesssim 3\%$ (measured from the internal dispersions ΔF_i), at the cost of reducing the sampling by a factor of 2. However, this is not an important loss, since the original 5000 Å sampling was at least twice as frequent as that in any other band. The revised data are tabulated in Paper III.

The multiwavelength variability data are shown in Figure 2. Light curves covering the entire 30 day time span for seven ultraviolet/infrared bands and four radio bands are given in Figure 2*a*. Data from the intensive satellite monitoring period (November 10.7–15.3), covering observing bands centered on 25 Å (PSPC), 1400 Å (SWP), 2800 Å (LWP) and 5000 Å (FES), are given in Figure 2*b*. Normalized variability amplitudes (NVA) are computed by taking all of the N data points in a given wave band and time span, and taking the ratio of the standard deviation over the mean. A crude measure of the error on each estimate is given by $\mathrm{NVA}/(N-1)^{1/2}$. These data are tabulated in Table 1, for a number of different observing bands and time spans.

Perhaps the most striking point in Table 1 is that the variability amplitudes appear constant from X-ray through infrared wavelengths, and then decline markedly to longer radio wavelengths. While this analysis is somewhat complicated by the

TABLE 1

ROOT MEAN SQUARE VARIABILITY IN DIFFERENT WAVE BANDS AND TIME SPANS

WAVE BAND (Å)	TOTAL		INTENSIVE		NONINTENSIVE		SECOND HALF	
	NVA (%)	N	NVA (%)	N	NVA (%)	N	NVA (%)	N
24	7.3 ± 1.3	33	7.3 ± 1.3	33				
1400	13.6 ± 1.4	98	5.4 ± 0.9	36	18.4 ± 2.8	45	7.5 ± 1.4	28
2800	14.3 ± 1.4	99	5.7 ± 0.9	39	20.0 ± 3.0	45	7.0 ± 1.5	23
3600	19.1 ± 2.6	54	9.0 ± 4.5	5	19.8 ± 3.0	46	8.1 ± 1.9	19
4400	17.8 ± 2.2	68	6.0 ± 2.7	6	18.2 ± 2.4	60	5.6 ± 1.3	20
5000	17.9 ± 2.0	84	6.0 ± 1.0	34	20.7 ± 3.5	36	6.9 ± 1.6	19
5500	18.2 ± 2.1	78	7.1 ± 2.5	9	19.1 ± 2.5	64	5.9 ± 1.3	23
6400	18.1 ± 2.2	66	6.0 ± 2.2	8	19.1 ± 2.6	54	5.8 ± 1.3	20
7900	18.5 ± 2.3	64	6.6 ± 2.5	8	20.1 ± 2.8	52	5.4 ± 1.3	19
12500.....	8.1 ± 2.3	13	...	...	...	...	7.2 ± 2.4	10
16500.....	6.5 ± 1.9	13	...	...	...	...	6.1 ± 2.0	10
22000.....	7.2 ± 2.1	13	...	...	...	...	6.4 ± 2.1	10
1.3×10^8.....	14.8 ± 5.6	8	...	...	13.6 ± 5.5	7	...	...
2.0×10^8.....	12.1 ± 4.3	9	...	...	11.7 ± 4.4	8	...	...
3.5×10^8.....	8.9 ± 3.2	9	...	...	9.0 ± 3.4	8	...	...
6.1×10^8.....	7.1 ± 2.7	8	...	...	7.2 ± 3.0	7	...	...
2.0×10^9.....	4.7 ± 1.8	8	...	...	4.5 ± 1.8	7	...	...

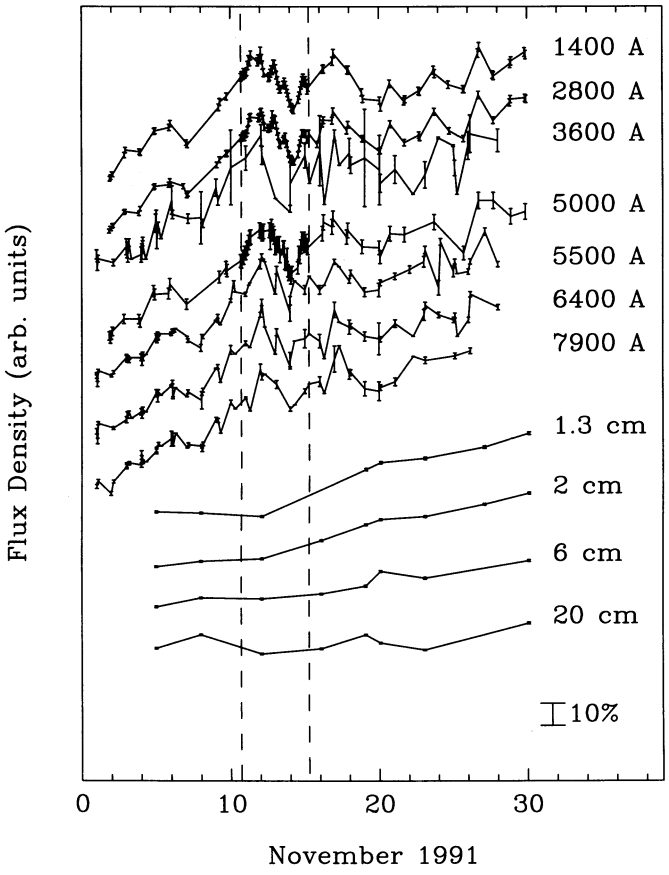

FIG. 2a

FIG. 2.—Multiwavelength light curves. The data for the entire 30 day observing period in seven ultraviolet/optical/infrared bands and four radio bands are given in (*a*). The dashed lines mark the intensive satellite monitoring period (1991 November 10.7–15.2). Light curves from this period, covering four observing bands centered on 25 Å (PSPC), 1400 Å (SWP), 2800 Å (LWP), and 5000 Å (FES).

fact that the different bands were observed over different timescales, a quantitative comparison can be made by restricting the analysis to bands and time spans in which the coverage is similar. For instance, during the period when both *IUE* and *ROSAT* observed PKS 2155−304 (November 12.2–15.1), all of the X-ray through optical bands showed a similar level of variability (~6.5%). During the second half of the campaign (November 16–31, the only period with good infrared coverage), the entire ultraviolet through infrared variability was again consistent with a single value of NVA ≈ 6.5%. Finally, restricting the analysis to those wave bands that spanned the entire month-long campaign and excluding data from the intensively sampled period (which could bias the amplitude of a well-sampled band relative to a poorly sampled one), the ultraviolet/optical data are again consistent with a single value (NVA ≈ 19%), but in the radio the level of variability decreases monotonically with wavelength, from 13.6% at 1.3 cm to 4.5% at 20 cm.

3. TIME-SERIES ANALYSIS

The first observational result of this campaign is that the variations in the different bands (except the radio) were all clearly correlated. The variations were sufficiently rapid that only the quasi-continuous data from the intensive monitoring

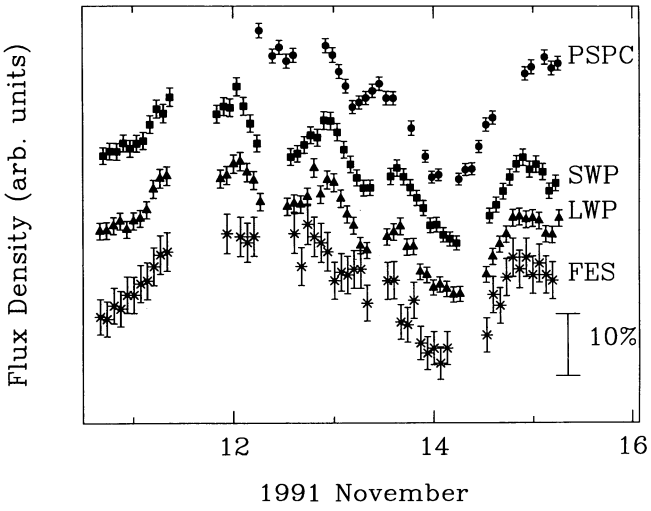

FIG. 2b

period were sampled rapidly enough to allow a detailed measurement of the correlation properties. For that reason, the correlation between the *ROSAT* 25 Å and *IUE* 1400 Å variations is examined in detail in § 3.1. The rest of the intensively sampled data are analyzed in § 3.2, and the optical through radio variations are discussed in § 3.3. Finally, the issue of possible periodicities in the data is discussed in § 3.4.

3.1. *Techniques for Measuring Lags*

In order to make quantitative estimates of the degree of correlation and the lag between variations at different wavelengths, four methods are applied to the relatively well-sampled 25 and 1400 Å data: the discrete correlation function (§ 3.1.1), a modification of the mean variance technique (§ 3.1.2), the χ^2 minimization technique (§ 3.1.3), and the maximum-entropy method (§ 3.1.4). The results are summarized and compared in § 3.1.5. In the following, a positive lag indicates that variations in the higher frequency continuum band leads those at lower frequencies, and a negative lag indicates the opposite.

3.1.1. *Discrete Correlation Function*

The discrete correlation function (DCF; Edelson & Krolik 1988) is analogous to the classical correlation function (which requires evenly sampled data), except that it can work with unevenly sampled data. It works as follows: First, the two unevenly sampled light curves, $x(t_i)$ and $y(t_j)$, are normalized to zero mean and unit dispersion:

$$x_i' = \frac{x(t_i) - \langle x \rangle}{\sigma_x}, \tag{1a}$$

$$y_j' = \frac{y(t_j) - \langle y \rangle}{\sigma_y}, \tag{1b}$$

where $\langle x \rangle$ and σ_x are the mean and standard deviation measured for the light curve $x(t_i)$. Then, for each pair of points x_i' and y_j', the time lag Δt_{ij} and unbinned DCF (UDCF) are computed:

$$\Delta t_{ij} = t_i - t_j, \tag{2a}$$

$$\mathrm{UDCF}_{ij} = x_i' y_j'. \tag{2b}$$

The UDCF are then binned in bins of width τ, such that for all N pairs with

$$T_{\mathrm{lag}} - \tau/2 < \Delta t_{ij} \leq T_{\mathrm{lag}} + \tau/2 \tag{3a}$$

the following is computed:

$$\mathrm{DCF}\ (T_{\mathrm{lag}}) = \frac{1}{N} \sum \mathrm{UDCF}_{ij}\ . \qquad (3b)$$

The result is the autocorrelation function when the input light curves are the same ($x_i = y_i$), and the cross-correlation function when they are different. As a final step, the best estimate of the lag is made with a three-point parabolic fit to the point with maximum correlation and the two adjacent points.

The 25–1400 Å cross-correlation function is shown in Figure 3. The highest point in the cross-correlation is at −1.80 hr, but the figure also shows a clear, double-peaked structure, with another peak of almost equal strength at +3.88 hr. This type of problem is often seen in the DCF, and it appears to be related to the fact that the measured function is a convolution of the lag with an autocorrelation function of nonzero width. PKS 2155−304 (like most AGN) appears to have a steep fluctuation power density spectrum (Tagliaferri et al. 1991), with significant power on timescales longer than the few days probed in the intensive sampling. This leads to a wide autocorrelation function, so the cross-correlation function is also very wide with a broad, flat peak, and thus is relatively insensitive to the exact value of the lag. To be conservative, we adopt the mean of the two peak values (+1.04 hr) as the best estimate of the lag.

At zero lag, the DCF is equivalent to the standard correlation coefficient [i.e., DCF ($T_{\mathrm{lag}} = 0$) = r], for which the significance can be simply calculated. These data can then be used to determine directly the probability that the data are in fact truly correlated. The values of r at zero lag and the associated false-alarm probability (p_0) are given in Table 2. This provides quantitative confirmation of what is probably obvious from examination of Figure 2, namely, that the ultraviolet/X-ray correlation is highly significant ($p_0 < 10^{-4}$).

However, this prescription cannot be used for nonzero lags, and systematic effects do not allow the DCF to measure meaningful errors across the entire function directly from the data, as was originally suggested by Edelson & Krolik (1988). Their error bars were measured by assuming that the UDCF points are independent, while in fact they are dominated by systematic effects introduced by the particular sampling pattern. In the case of evenly sampled observations, such as the ultraviolet monitoring of NGC 5548 (Clavel et al. 1991), the errors are overestimated, while for unevenly sampled light curves (e.g., Edelson, Krolik, & Pike 1990) the errors are clearly underestimated. Because the errors on the points are not reliable, and in any event the goal of correlation analysis is generally to measure the errors on the lag, not on the value of the correlation function at a given lag (which the DCF does not directly provide), another method must be used to estimate the errors.

Therefore, Monte Carlo simulations are used to estimate the error on the lag and to determine whether it is significantly different from zero, as follows: First, identical synthetic 25 and 1400 Å light curves are produced with the same statistical characteristics as the observed ones. A fluctuation power density spectrum with a power-law slope of $P(f) \propto f^{-2}$ [where $P(f)$ is the fluctuation power at temporal frequency f] is assumed. Although the interruptions make this data set unsuitable for measuring the slope of the power density spectrum, previous X-ray measurements by Tagliaferri et al. (1991) indicate a slope of about −2. Next, the variability amplitudes are normalized to those observed (7.3% for the 25 Å data and 5.4% for the 1400 Å data). Then the synthetic data are sampled at the same times as the observed data, and Gaussian noise added at the measured noise level (1% for the 25 Å data and 1.5% for the 1400 Å data). The cross-correlation is then derived, and the best estimate of the lag is measured, in the same fashion as the observed data. This process is repeated to produce 10,000 independent tests, and the confidence range is taken to be that containing 90% of the test lags. A histogram of the results is shown in Figure 4.

These simulations yielded a 90% confidence interval of −6.66 to +3.74 hr. Only about half the test runs yielded lags outside the range ±1.04 indicating that the lag, as measured by the DCF was not significantly different from zero.

3.1.2. *Modified Mean Deviation Technique*

The second method used in this study is a modification of the mean variance method introduced by Hufnagel & Bregman (1992). It assumes that the two light curves are

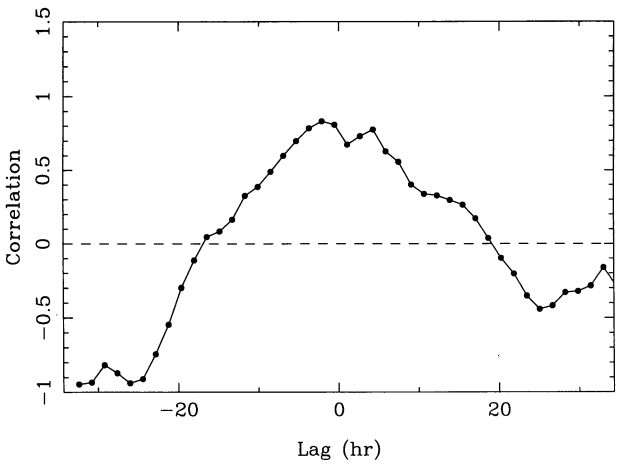

FIG. 3.—Discrete correlation function between 25 and 1400 Å. The sense of the effect in this and all of the figures is that a maximum (or, for the MMD and χ^2 methods, a minimum) at positive lags means that the shorter wavelength variations lead those at longer wavelengths. The best estimate of the lag is the average of the two peaks, +1.04 hr. The errors are determined in Fig. 4.

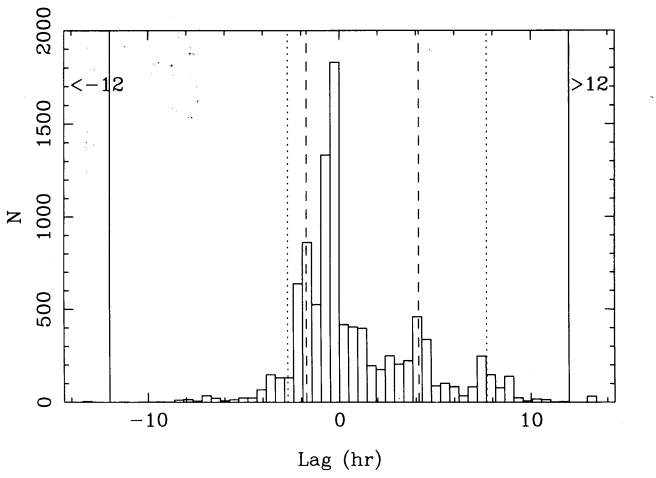

FIG. 4.—Histogram of results of Monte Carlo simulations to determine the errors on the DCF 25–1400 Å lag. In this and all of the following histograms, the dashed line represents the 1 σ (67%) confidence level, the dotted line represents the 90% confidence level, and the data outside the solid lines at ±12 hr all lie outside the plot range. Note that since the goal of the simulations is to determine whether the measured lag is consistent with zero, the axes appear to run opposite to those in Fig. 3 and the errors in Table 2. In this figure the 1 σ errors are so large that the measured lag is consistent with zero.

actually realizations of the same process, but shifted in time and flux level. Thus, it cannot be used to estimate the significance of the correlation between wavelengths.

This modified mean deviation (MMD) method works as follows: First, the two unevenly sampled light curves, $x(t_i)$ and $y(t_j)$, are normalized to zero mean and unit dispersion, to yield x_i' and y_j' as above. Then, for each pair, the lag Δt_{ij} and flux difference ΔF_{ij} are computed:

$$\Delta t_{ij} = t_i - t_j \,, \tag{4a}$$

$$\Delta F_{ij} = x_i' - y_j' \,. \tag{4b}$$

The ΔF_{ij} are then grouped into ranges of Δt_{ij} such that for all of the N pairs with

$$T_{\rm lag} - \tau/2 < \Delta t_{ij} \leq T_{\rm lag} + \tau/2 \tag{5a}$$

the following are computed:

$$\langle \Delta F \rangle = \frac{1}{N} \sum \Delta F_{ij} \,, \tag{5b}$$

$$\mathrm{MMD}(T_{\rm lag}) = \sigma_{\Delta F} = \left[\frac{1}{N} \sum (\Delta F_{ij} - \langle \Delta F \rangle)^2 \right]^{1/2} . \tag{5c}$$

Finally, as with the DCF, the best estimate of the lag is made with a parabolic fit.

The results are shown in Figure 5. There is no "double peak" seen with the MMD method. Errors on the lag are estimated in the same fashion as with the DCF (see Fig. 6). The best estimate of the lag is +2.84 hr, and the 90% confidence interval is −6.22 hr to +6.21 hr. Thus, the simulations show that the lag measured by the MMD method is not significantly different from zero.

3.1.3. χ^2 *Minimization Technique*

The third method is an adaptation of a technique developed for the analysis of time delays in the light curves of the gravitational lens 0957+561. Like the MMD technique, this method assumed that the light curves have the same underlying correlation properties, so it cannot be used to test the strength or significance of the correlation. In principle, it allows analytic estimation of the errors on the lag. Details are given in Press, Rybicki, & Hewitt (1992).

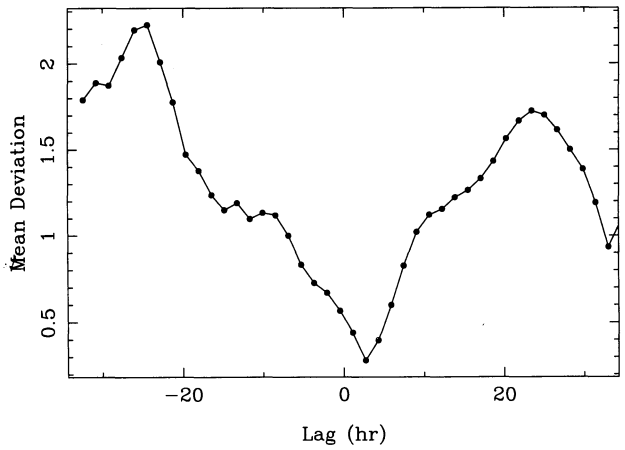

FIG. 5.—MMD analysis between 25 and 1400 Å. The best estimate of the lag is the minimum point, with the X-rays leading the ultraviolet by +2.84 hr. Errors are estimated by Monte Carlo simulation in Fig. 6.

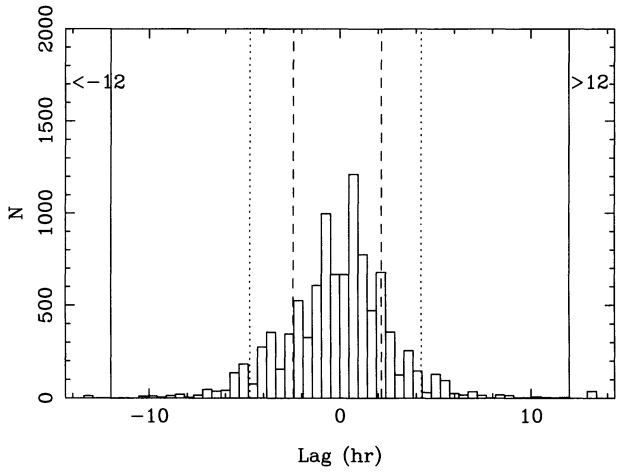

FIG. 6.—Histogram of results of Monte Carlo simulations to determine the errors on the MMD 25–1400 Å lag. Again, the results are consistent with zero lag.

As before, the data are normalized to zero mean and unit variance. Then the one-point estimate of the structure function, v_{ij}, is calclated for all pairs of points:

$$\Delta t_{ij} = |t_i - t_j| \,, \tag{6a}$$

$$v_{ij} = \tfrac{1}{2}(x_i' - x_j')^2 - \tfrac{1}{2}\epsilon_i^2 - \tfrac{1}{2}\epsilon_j^2 \,, \tag{6b}$$

where ϵ_i is the fractional error on the measurement x_i'. The structure function, of the form $V(\tau) = b|\tau|^\gamma$, is fitted after binning the v_{ij} into equal-size bins. Since the analysis assumes that the structure functions are identical for all light curves, the parameters used in the time-delay analysis are the average of the fitted parameters. These structure-function fit parameters for the different light curves are in fact very similar, and in any event the time-delay measurement is insensitive to the values assumed.

The two light curves are then combined to form a single light curve, assuming a flux ratio and time delay. The statistical properties of this joint light curve are compared with those of the individual light curves by calculating the generalized χ^2 statistic, defined as

$$\chi^2 = \sum x_i' A(\Delta t_{ij}) x_j' \,, \tag{7}$$

where $A(\Delta t_{ij})$ is the inverse of the total covariance matrix:

$$A(\Delta t_{ij}) = [\sigma^2 - V(\Delta t_{ij}) - \tfrac{1}{2}(1 - \delta_{ij})(\epsilon_i^2 + \epsilon_j^2)]^{-1} \,, \tag{8}$$

and where σ^2 is the unknown population variance of $x(t)$. By taking the limit, $\sigma^2 \to \infty$, the dependence on the population variance is removed. When the generalized χ^2 is minimized, the assumed time delay and flux ratio yield maximum-likelihood estimates of the true time delay and flux ratio. In other words, when the assumed time delay and flux ratio approximate the true delay and ratio, and joint light curve should exhibit the same correlation properties as the individual light curves, provided that the original assumption, that the two light curves are drawn from the same parent light curve, is correct.

Since this statistic is not a true χ^2 statistic (Press et al. 1992), the confidence intervals are determined by Monte Carlo simulation as before. The resulting plot of χ^2 as a function of delay is presented in Figure 7. The best estimate of the lag is +2.28 hr, and the 90% confidence interval is +1.68 to +3.53 hr, in the sense that the X-rays lead the ultraviolet. The simulations

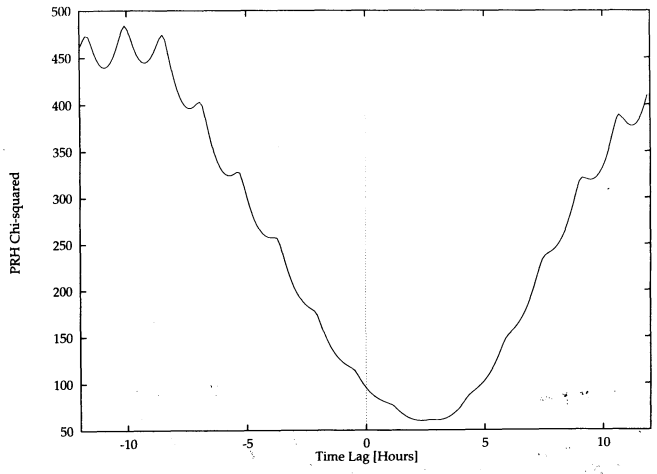

FIG. 7a

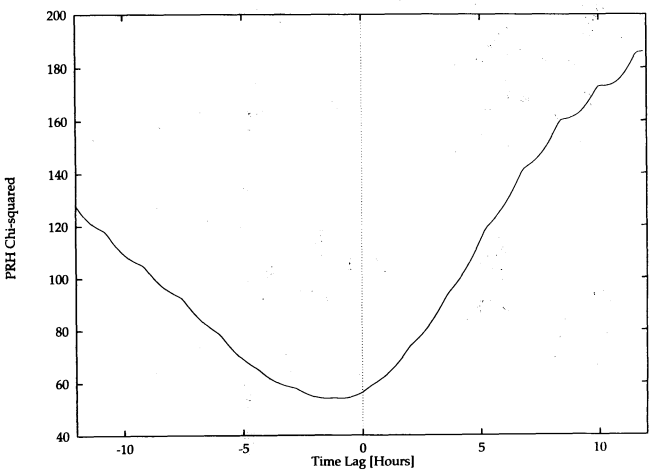

FIG. 7c

FIG. 7.—(*a*) χ^2 analysis between 25 and 1400 Å, (*b*) 1400 and 2800 Å, and (*c*) 2800 and 5000 Å. The data indicate that the X-rays lead the ultraviolet by a significant amount (~2–3 hr), while no significant lag can be measured between the other bands.

show that the lag measured with the χ^2 method is significantly different from zero at approximately the 5 σ level. Thus, for this problem, the χ^2 method is more powerful than the DCF or MMD methods, and it shows that the X-rays lead the ultraviolet by a significant amount.

3.1.4. *Maximum-Entropy Technique*

The final method used to estimate the lag was the maximum-entropy method (MEM). MEM tries to find both a "smooth" X-ray light curve that fits the 25 Å data points and "smooth" transfer functions that, when convolved with the X-ray light curve, give a light curve that fits the 1400 Å points. In this approach, the 1400 Å light curve is modeled as a linear convolution of the X-ray light curve with a transfer function. The transfer function then gives the time-delay distribution of the ultraviolet variations with respect to the X-ray variations. Details of the method, used previously to measure transfer functions between line and continuum variations of Seyfert 1 galaxies, may be found in Horne, Welsh, & Peterson (1991) and Krolik et al. (1991).

Figure 8 shows the MEM reconstructions of transfer functions obtained for the 1400, 2800, and 5000 Å light curves measured with respect to the 25 Å light curve. (Unlike the previous methods, the MEM permits simultaneous analysis of more than two light curves.) A two-parameter family of satisfactory solutions is examined to fit the data with reduced χ^2 values of 1.0–0.5. In all of these solutions, the peak of the 1400 Å transfer function occurs at a delay of ~2.5 hr. The transfer function has a full width at half-maximum of 2.5–7.5 hr. This range indicates that the width of the transfer function is not tightly constrained by these data. No attempt is made to estimate quantitatively the errors on the MEM results with Monte Carlo simulations.

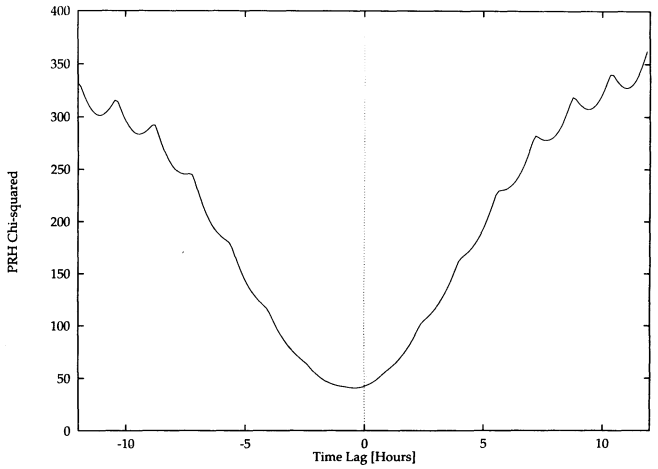

FIG. 7b

3.1.5. *Summary, Comparisons, and Caveats*

The results of the 25–1400 Å correlation analyses are summarized in the first line of Table 2. Note that the errors refer to 90% confidence intervals. The DCF (the only method tested that is sensitive to the strength of the correlation) confirms that all of the light curves are strongly correlated. The χ^2 method

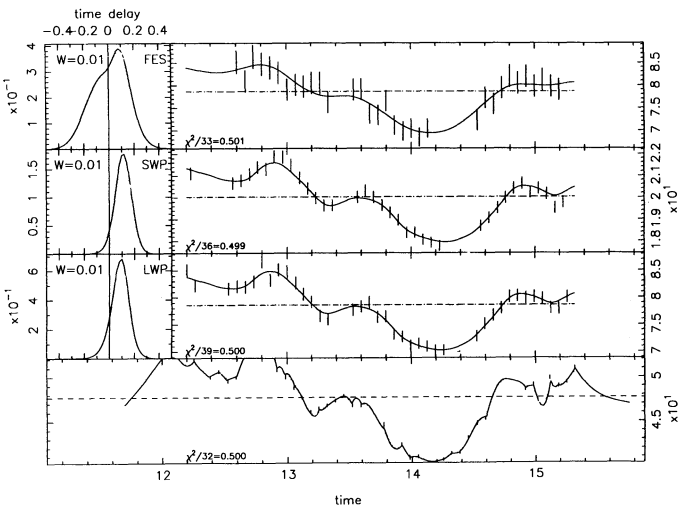

FIG. 8.—Results of MEM analysis. The bottom panel shows the X-ray light curve fitted through 25 Å observations (vertical error bars). On the right-hand side of the upper three panels, the 5000, 2800, and 1400 Å data (*vertical error bars*) are used to constrain and fit a light curve resulting from convolution of the X-ray light curve from the bottom panel with the transfer function shown on the left-hand side. This fit has a reduced χ^2 of 0.5.

TABLE 2

CORRELATIONS AND LAGS

Wave Bands (Å)	$r_s(0)$	$N(0)$	$p(0)$	DCF Lag[a] (hr)	MMD Lag[a] (hr)	χ^2 Minimum Lag[a] (hr)	MEM Lag (hr)
24–1400.....	0.79	22	$<10^{-4}$	$+1.04^{+2.70}_{-7.70}$	$+2.84^{+3.37}_{-9.06}$	$+2.28^{+1.25}_{-0.60}$	+2.5
1400–2800.....	0.93	51	$<10^{-4}$	$+0.48^{+4.70}_{-4.27}$	$+0.20^{+5.23}_{-3.96}$	$-0.48^{+0.84}_{-0.96}$	0
2800–5000.....	0.84	48	$<10^{-4}$	$-2.76^{+10.0}_{-14.7}$	$-0.31^{+43.7}_{-40.0}$	$-0.96^{+1.20}_{-1.92}$	0

[a] Note that the quoted errors are 90% confidence intervals.

found that the lag of ~2–3 hr is significant at approximately the 5 σ level. The other three methods yield similar values for the lag, but the significance is lower (~1.5 σ). Thus, for this experiment, the χ^2 method proved to be the most powerful. However, no one method is best in all cases, and another approach may prove more useful under different circumstances.

An unfortunate defect of this data set is the presence of gaps in the otherwise even sampling. In particular, gaps occur in the 25 Å coverage around November 12.8 and 14.8, just prior to two of the three local maxima in the 1400 Å light curve (although the minima in both light curves are well defined). The MEM fit introduces unobserved X-ray flares in the 25 Å data gaps in order to produce the observed maxima in the 1400 Å light curve while retaining rather broad transfer functions. The other methods must also effectively do this as well.

The data near the end of the experiment appear to diverge, with the 1400 Å fluxes declining from a maximum while the 25 Å flux is rising. MEM makes a rather strained fit to this difficult section by means of a flare in the data gap around November 14.8 and a dip between the two 25 Å measurements around November 15.05. This suggests that the true relationship between the X-ray and ultraviolet variations could be more complicated than a simple linear convolution, and that while the light curves are strongly correlated on short timescales, they may diverge when timescales longer than the ~3 days sampled in the intensive period are probed.

Such behavior could indicate that there is a hierarchy of size and timescales, in which case the measured lag could depend on the length of the monitoring campaign. For instance, consider what would happen if the same process operates in two regions of different size, with the larger region having larger amplitude variations, longer lags, and longer variability timescales. Then, if one monitored for only a short time, one would only be sensitive to the small, rapid variations from the smaller region, and the shorter lag would be measured. However, if one monitored for long times, the larger amplitude variations would dominate, and the larger lag would be found. In both cases the direction of the lag is the same if both regions emit by the same process. Thus, this experiment gives greater confidence in the sign of the lag (which indicates whether the X-rays or ultraviolet lead) than in its magnitude.

This is the first measurement of the temporal correlation between X-ray and lower energy variations from any BL Lac object, and the first indication that X-ray variations precede those at lower energies. This has very important implications for emission models, as discussed in § 4.

3.2. *Correlations Measured with the Intensively Sampled IUE Data*

The intensively sampled 1400–2800 Å and 2800 Å correlations were analyzed in a fashion identical to the 25–1400 Å correlations. These results are presented in lines 2 and 3 of Table 1 and in Figures 9 and 10. For the correlations involving only *IUE* data (1400–2800 Å and 2800–5000 Å), slightly longer timescales are covered, and the Monte Carlo simulations assumed errors of 1.5% at 1400 and 2800 Å and 3% at 5000 Å, and NVAs of 6.2%, 5.7%, and 6.0% at 1400, 2800, and 5000 Å, respectively.

Again, the DCF confirms that all of the light curves are strongly correlated. For both the 1400–2800 Å and 2800–5000 Å correlations, all the methods yield results consistent with no lag, within limits of $\lesssim$1–2 hr in the most constraining analysis (the χ^2 technique).

3.3. *Lower Frequency Correlations*

Extending these results to lower frequencies and longer timescales is more difficult. This is not because there are not enough data. With $N \approx 65$ in a number of optical bands, there are actually more data than the $N = 35$–50 points used in the ultraviolet/X-ray analyses. Rather, the problem is that the lower frequency data lack the homogeneity and relatively even sampling of the intensive satellite monitoring. The ground-based data in any given band consist of observations made with many different telescopes, detectors, calibration sources, and reduction techniques. (See Paper III for a detailed discussion of these data.) Although each of the data sets contributing to this large database may be internally consistent, systematic differences between different observers' data could greatly affect the result. Since there is no obvious, reliable way to weight these data or estimate errors by Monte Carlo simulation, only qualitative analyses are given.

Visual inspection of the month-long light curves (Fig. 2) suggests a correlation throughout the ultraviolet/optical/infrared regime. All of the ultraviolet/optical data appear strongly correlated, with no significant evidence for a lag greater than the typical sampling limit of ~1 day. The infrared data have even poorer sampling, with only 8–13 points, but again appear to follow closely the trend in the high-frequency data.

The sparsely sampled radio data to not show this correlation at zero lag, however. The radio data can be crudely described as staying roughly constant for the first half of the campaign and then rising somewhat in the second half. The rise appears to occur later and become progressively weaker as one goes from 1.3 cm to longer wavelengths, with very weak variability and no obvious trend at 20 cm, the longest wavelength band sampled. The long-term optical/ultraviolet light curve rises in the first 10 days of the campaign and remains at a high level for the last 20 days. It does appear that the radio variations could be related to but lagging the optical/ultraviolet by ~5–10 days, with shorter delays and stronger correlations at the shorter radio wavelengths. Unfortunately, the lack of millimeter/submillimeter data make it impossible to track the

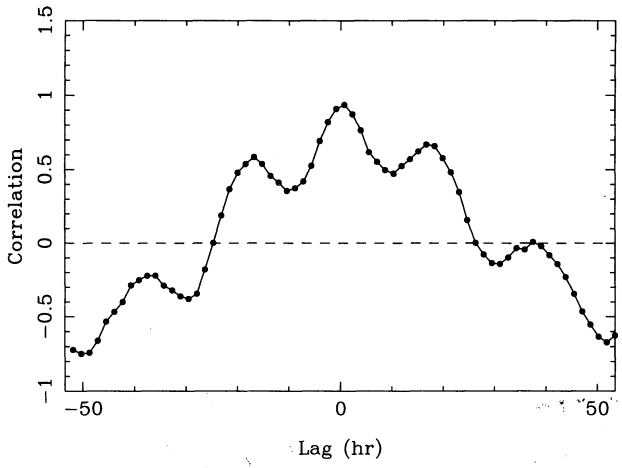

FIG. 9a

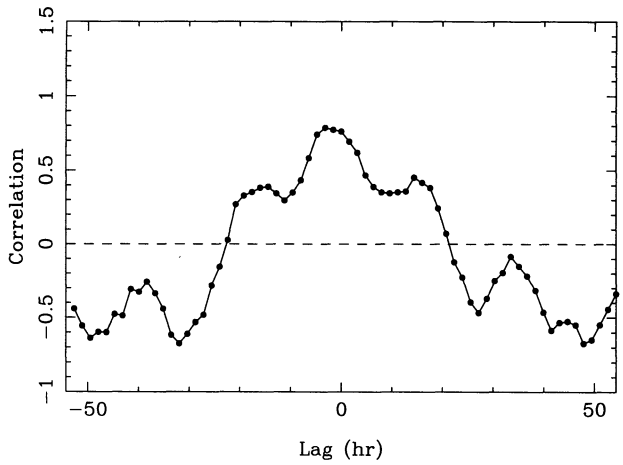

FIG. 9b

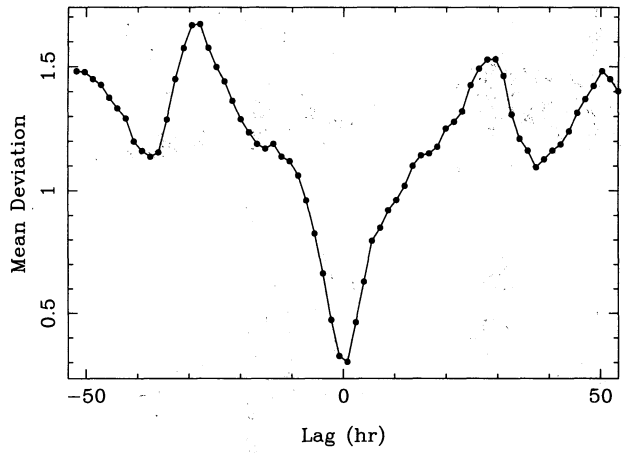

FIG. 9c

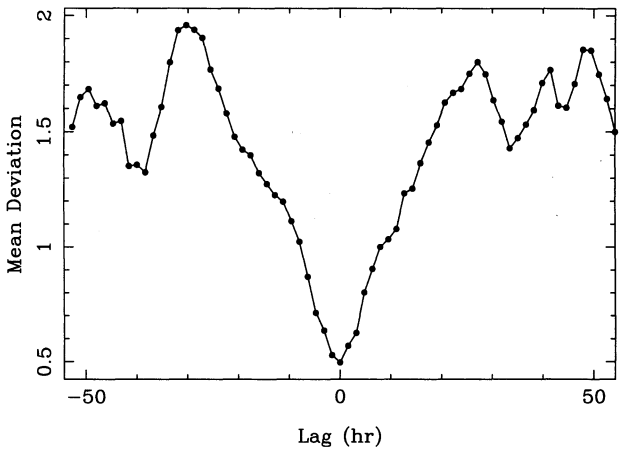

FIG. 9d

FIG. 9.—Analysis of ultraviolet/optical correlations in the intensively sampled data. The 1400–2800 Å correlations are on the right, and the 2800–5000 Å correlations are on the left. In the DCF analysis on the top, the best estimate of the lag is the maximum value of the function, while in the MMD analysis on the bottom the best estimate is the minimum.

lag and tell with certainty whether this behavior is connected to the variations seen at higher energies.

3.4. *Periodicity Analysis*

Detection of a periodic component to the variations would be of great importance, arguing against beaming and for a more isotropic emission source, such as an orbiting source or a hot spot on a disk. Figure 11 shows the autocorrelation functions for the intensively sampled data, measured with the DCF technique. The autocorrelation functions derived from the *IUE* observations appear to have shoulders at ~0.7–0.8 days (Paper I). However, as mentioned previously in this paper, errors generated by the DCF are not meaningful, so the significance of any potential periodicity cannot be accessed by examination of the autocorrelation function alone. Therefore, this paper employs a procedure designed specifically to detect periodicity in the presence of noise.

There are two general types of statistical methods which have been used to search periodicities. The first and most widespread uses Fourier techniques to measure the power spectrum (e.g., Bracewell 1986), and as such is not directly applicable to these unevenly sampled data. (For example, directly transforming the DCF autocorrelation function would yield a highly corrupted power spectrum.) The second method, folding the data on test periods, can be applied to unevenly sampled data, and is also more sensitive to nonsinusoidal pulse shapes that might be seen in AGN.

In this paper, the epoch-folding Q^2 statistic of Daves (1990) is used. This method, which has already been used to test for periodicities in AGN (e.g., Done et al. 1992; Leighly et al. 1994), is well suited for detecting periodic modulation in the presence of both erratic variability and measurement noise. It tests the hypothesis that there is no periodic signal with a given period: First, the N data points are folded on a trial period and binned by phase. For the ith of M phase bins, the mean x_i and sample variance σ_i^2 are computed, as is the overall mean, $\langle x \rangle$. Then the Q^2 statistic is computed,

$$Q^2 = \sum_{i=1}^{M} \frac{(x_i - \langle x \rangle)^2}{\sigma_i^2} . \tag{9}$$

Q^2 is distributed similarly to the χ^2 statistic. The false-alarm probability (the confidence with which one can reject the null hypothesis) can be determined from

$$L = \frac{(N - M)Q^2}{(M - 1)(N - 1) - Q^2} , \tag{10}$$

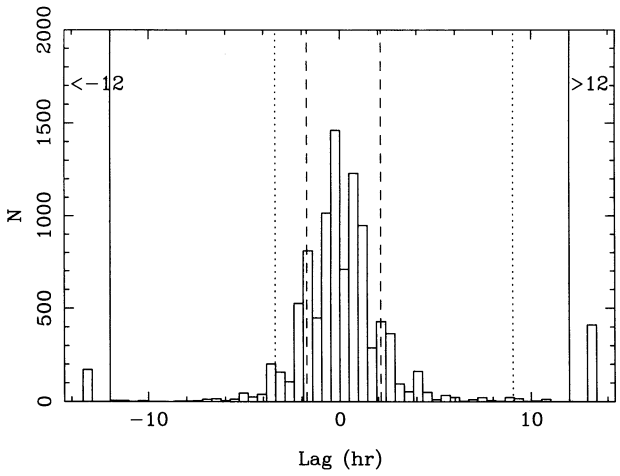

FIG. 10*a*

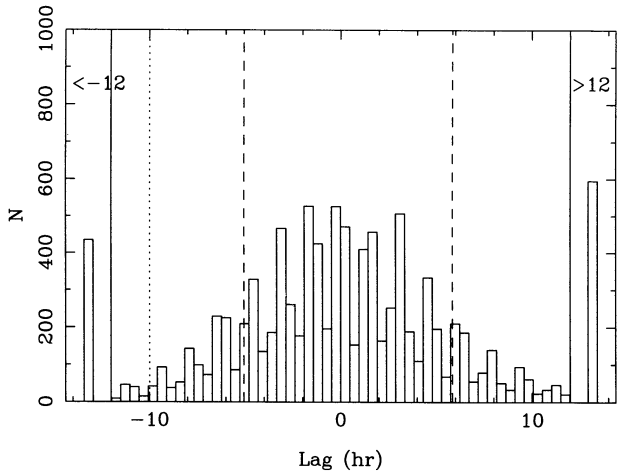

FIG. 10*b*

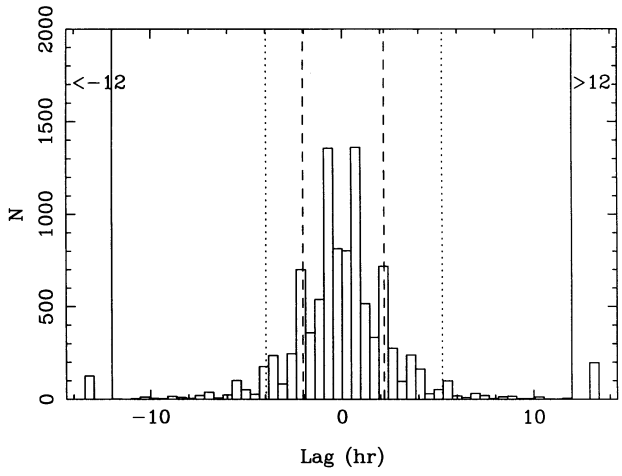

FIG. 10*c*

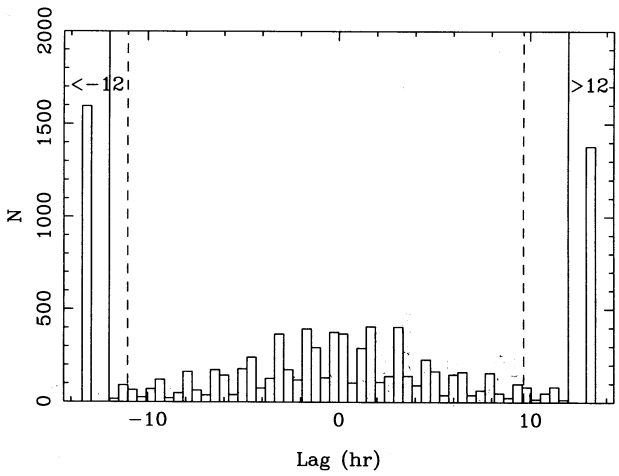

FIG. 10*d*

FIG. 10.—Histogram of Monte Carlo simulations corresponding to the correlation functions in the preceding figure. The dashed line refer to the 1 σ confidence intervals, and the dotted lines to the 90% confidence intervals. These simulations show that neither the DCF (*top*) nor the MMD (*bottom*) methods find any significant lag, either for the 1400–2800 Å (*left*) or the 2800–5000 Å (*right*) bands.

where L has an F distribution with $M - 1$ and $N - 1$ degrees of freedom.

The intensively sampled 25, 1400, 2800, and 5000 Å light curves are sampled fairly regularly (but with interruptions totaling about a third of the time) for 2.3–4.5 days. This test has been done for these four data sets, and the results are plotted in Figure 12. (The sampling frequency and homogeneity of the ground-based data are insufficient for meaningful periodicity analysis.)

For the three ultraviolet/X-ray light curves, the confidence level at which one can reject the hypothesis that the source is periodic is $p_0 = 30\%–50\%$, while for the most significant case, the 5000 Å data, the confidence level is $p_0 = 13\%$. These are not statistically significant. By comparison, the application of this technique to the X-ray data on NGC 6814 by Leighly et al. (1994) found that source to have a periodic component at the $p_0 \ll 10^{-50}$ confidence level, and even the initial, less powerful analysis by Mittaz & Branduardi-Raymont (1989) was significant at the $p_0 \lesssim 3\%$ level. Thus, this statistical test shows no evidence for periodicity in any of the light curves.

An alternative, nonstatistical approach is to time the maxima and minima in the light curves. Application of this technique to the 1400 Å light curve, for instance, shows four clear maxima (at November 11.97–12.10, 12.90–12.97, 13.57–13.70, and 14.83–14.96) and three clear minima (at November 12.23–12.57, 13.30–13.37, and 14.23–14.56). (The large gap at November 11.36–11.83 makes it impossible to determine whether and when any earlier changes of direction occurred.) Because the data have such high signal-to-noise ratios, the times of these minima and maxima are fairly well defined. There is no single periodic function consistent with all these times. For instance, a 0.8 day periodicity is consistent with the first three maxima, but would predict a peak at or near November 14.50, when the source is actually in a minimum.

There are two possible reasons why the *IUE* autocorrelation functions showed features (Paper I) which are not confirmed by the more rigorous analyses herein. First, the *IUE* data were subjected to ~0.2–0.3 day interruptions by Earth occultation at the same time each day. The average span of uninterrupted observations was 0.7–0.8 days, resulting in a window function

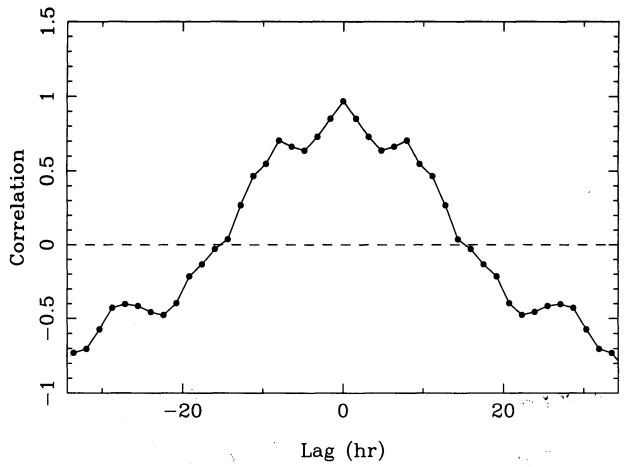

FIG. 11*a*

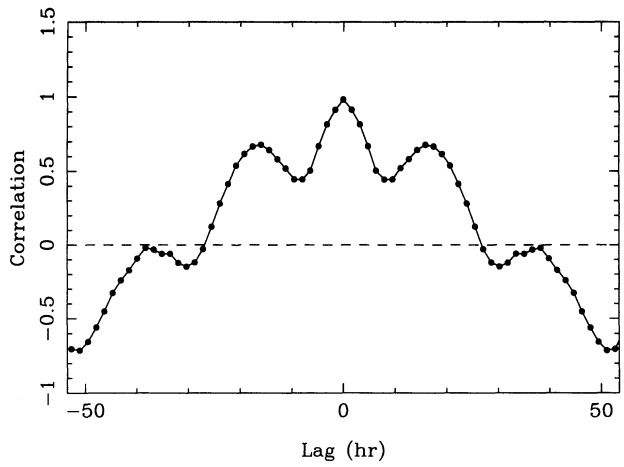

FIG. 11*b*

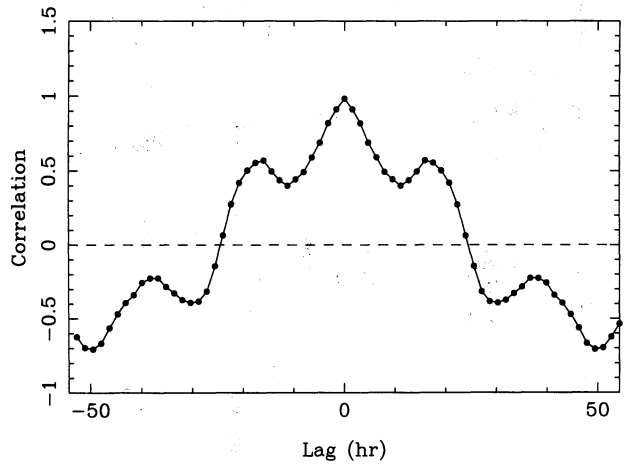

FIG. 11*c*

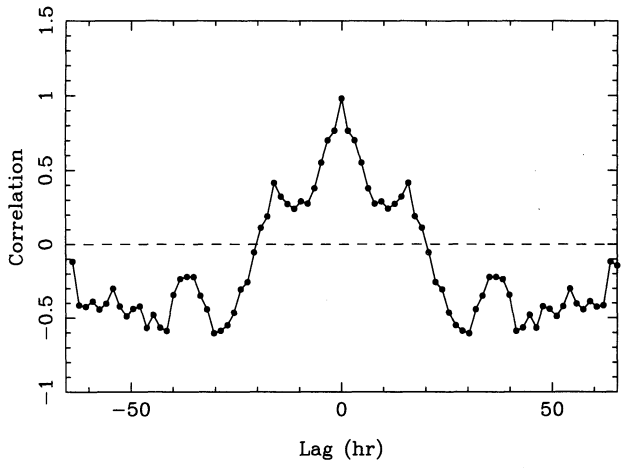

FIG. 11*d*

FIG. 11.—Discrete autocorrelation function at (*a*) 25 Å, (*b*) 1400 Å, (*c*) 2800 Å, and (*d*) 5000 Å

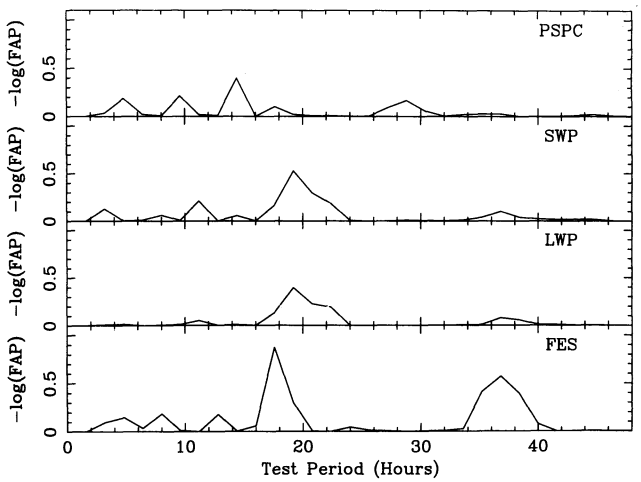

FIG. 12.—Results of the epoch-folding tests for the 25, 1400, and 2800 Å data. The ordinate is the log of the inverse of the false-alarm probability (FAP) (the confidence level). Thus, a value of 0.3 would mean that the hypothesis that the variability is periodic could be rejected at the 50% confidence level, while a value of 1.3 would mean that it could only be rejected at the 5% confidence level (i.e., a higher probability of periodicity).

with a spike at this timescale. Since AGN show strong variability over many timescales, the poor window function can irretrievably alias variability power to this particular timescale.

Second, the eye tends to pick out spurious apparent periodicities in erratically variable sources (such as AGN), at timescales a few times shorter than the total observation time. To quote Press (1978), "The strongest period in (actually nonperiodic) data will be about one-third the length of the data sample. In astronomy, one might to well to take 'three-period' quasicycles with more than a grain of salt." (See also Mandelbrot 1969.) That referred to coverage with no gaps. During the intensive *IUE* monitoring period of November 10.7–15.2, the source was actually observed only about two-thirds of the time, with other sources being observed during the remaining time, so the effective period was 4.5 days $\times \frac{2}{3} = 3$ days. Thus, timescales of order 1 day are suspect.

Thus, there is no compelling evidence for periodic behavior in these data. Furthermore, these results do not support the hypothesis (Paper I) that the variations in PKS 2155−304 have a "quasi-periodic oscillator" (or QPO) character similar to that seen in X-ray binaries (e.g., van der Klis 1989). In QPOs, the fundamental temporal frequency of the periodicity is not fixed at a single, constant value. Instead, it wanders

slowly around a mean value. However, for these sources, the apparent temporal frequency of the periodicity does remain approximately stationary over a small number (less than 10) of cycles. This would produce an apparently sharp and detectable periodicity, which was not seen. Of course, the possibility of QPOs cannot be completely eliminated, since one could always posit changes in the peak temporal frequency which would be too rapid to detect, or a fundamental temporal frequency that is too low to detect in this finite data train. However, these data give no positive evidence for such QPO behavior.

4. DISCUSSION

Several mechanisms have been proposed to explain the broadband properties of BL Lac objects. These include synchrotron radiation and self-Compton scattering by relativistic electrons in a jet or shock front, Compton scattering on "external" photons, nonrelativistic Compton scattering ("Comptonization"), thermal bremsstrahlung from the inner region of an accretion disk, and microlensing by an intervening galaxy. In this section, the results of the multiwavelength monitoring of PKS 2155−304 are compared with the predictions of these models.

4.1. *The Synchrotron/Compton Models*

Following the suggestion that the emission observed from BL Lac objects could be produced within a collimated jet and enhanced by relativistic beaming (Blandford & Rees 1978), a number of authors have studied relativistic jet models. The basic emission mechanisms studied are synchrotron and Compton radiation (see, e.g., Königl 1989 and references therein). In these models, the low-frequency spectrum (up to the optical/ultraviolet band) is attributed to synchrotron radiation from relativistic electrons, while, depending on the specific assumptions about the physical quantities in the jet, either synchrotron emission or Compton scattering could produce the X-rays. These models have been quite successful in reproducing the spectral properties of BL Lac objects. However, they have a relatively large number (~ 10) of free parameters, and the physical conditions cannot be very strongly constrained by single-epoch spectra alone.

4.1.1. *Compton Scattering*

The first issue that can be clearly addressed with these data is whether the soft X-ray emission seen with *ROSAT* can be produced by the Compton upscattering of lower energy photons. If a single homogeneous source of relativistic electrons provides the lower energy seed photons (via the synchrotron process) which are then upscattered (i.e., the synchrotron–self-Compton, or SSC, process), then the X-ray variations should occur either after or at the same time as lower energy variations. Thus, the simplest SSC model cannot account for the soft X-ray emission (in the 0.2–2 keV band), since it *leads* the lower energy variations.

Consider further whether the seed photons could be derived from some independent source. If the relativistic electrons responsible for upscattering these photons to soft X-ray energies were the same as those which produce the radio through ultraviolet synchrotron spectrum, the Compton radiation should have roughly the same spectral slope as the longer wavelengths ($\alpha = +0.01$ to -0.79). However, it is much steeper in the X-rays ($\alpha = -1.65$) than in any lower frequency band (see Fig. 1 and Paper II), arguing against this hypothesis.

However, these data do not address the importance of Compton scattering at energies higher than those probed by *ROSAT* (above 1 keV). In particular, Compton scattering is often invoked to explain the high-energy γ-rays from blazars (Maraschi, Ghisellini, & Celotti 1992), a conclusion that is not contradicated by these results.

Finally, it should also be kept in mind that PKS 2155−304 is an *X-ray*–selected BL Lac object, the subclass for which synchrotron emission is thought to be most dominant. This experiment does not address the question of the role of Compton scattering in *radio*-selected BL Lac objects a subclassification for which it has been argued that Compton scattering is more important (Maraschi 1992).

4.1.2. *Synchrotron Emission*

4.1.2.1. General Constraints

As mentioned earlier, it is most commonly assumed that the radio through ultraviolet SEDs of BL Lac objects are produced by direct synchrotron emission. In the present case, the spectral continuity and synchronous variations (within a few hours) at infrared through ultraviolet frequencies are in agreement with this general view. The strong X-ray/ultraviolet correlation, when combined with the fact that the X-rays lead the ultraviolet, argues that the X-rays would also be produced by direct synchrotron emission. This would require that the electron energy distribution extend to higher energies than would be necessary to produce only the radio through ultraviolet SED. This means that γ_{max} would have to increase by an order of magnitude, for a fixed magnetic field strength.

Another general constraint derives from the absence of strong X-ray spectral variability (e.g., Paper II). Reasonable estimates of the lifetimes for the X-ray–emitting electrons are very short (e.g., ~ 0.01 s; see § 4.1.2.2). Since the ultraviolet and X-ray light curves are so similar, the temporal behavior must be dominated by the energy input mechanism in essentially one region, with frequency-dependent geometry playing a secondary role. That is, the electrons would need to be continually reaccelerated in situ, because any electron distribution derived from a single injection would quickly steepen, producing significant spectral changes.

Finally, the 2–3 hr lead of the X-rays with respect to the lower frequencies is much shorter than the fastest variation seen in any band. If the variability timescales are related to the size of the emitting regions, the short lag could be caused by Doppler foreshortening and phase effects in the direction of motion of the plasma or perturbation and/or to a flattened geometry (e.g., a shock front in a jet oriented toward us; see § 4.1.2.3).

4.1.2.2. Tampered Jet Model

Marscher (1980) and Ghisellini et al. (1985) explained the basic shape of the SED of blazars as emission from a tapered jet. The flow could accelerate from its base, where the highest frequency synchrotron emission is produced, to the site of the radio emission (Ghisellini & Maraschi 1989). In this model, the magnetic field and relativistic electron energies decrease with distance down the jet, as the transverse size of the emission region increases. An increase in the flow of energy down the jet would lead to a flare seen first at higher and later at lower frequencies. In the context of this model, the observation that the X-rays lead the longer wavelengths suggests that the innermost synchrotron-producing region is radiating at X-ray or higher energies, and qualitatively conforms with expectations.

However, this model has difficulties explaining both the magnitude of the ultraviolet/X-ray lag and the lack of spectral variability. To estimate the range of physical conditions required by this model, the broadband SED of PKS 2155−304, shown in Figure 1, was fitted with the relativistic jet model described in Ghisellini et al. (1985). A bulk relativistic velocity of $\Gamma = 10$ was assumed, although the true number could be either higher (Melia & Königl 1989) or lower (Ghisellini & Maraschi 1989). In this model, the jet starts with a dimension of 3×10^{13} cm and extends with parabolic shape to 3×10^{16} cm, which is the dominant region for emission above 10^{13} Hz. At lower frequencies, the emission is self-absorbed and the jet structure is assumed to change to a conical shape (not included in the fit shown). The magnetic field at the core of the jet is $B \approx 3000$ G, corresponding to a maximum electron energy of $\gamma \approx 5000$.

This implies that the high-energy electrons emitting in the X-rays will have very short radiative lifetimes ($t_{1/2} \approx 0.01$ s). As mentioned earlier, the electrons responsible for the X-ray variations cannot also produce the ultraviolet variations unless they are reaccelerated. Likewise, if a shock traveling down the jet is responsible for the variations, it would have to travel $\sim 10^{16}$ cm to reach the ultraviolet-emitting region. This corresponds to a light travel time of ~ 4 days. Extremely large relativistic corrections would be needed to make this compatible with the observed lag of 2–3 hr.

Furthermore, Celotti, Maraschi, & Treves (1991) computed simulated light curves that would be expected in such a model, approximating the propagation of a shock wave in the jet by a schematic perturbation of given size and amplitude moving at constant speed (but without making relativistic corrections to the timescales). They predicted strong spectral variability, with the X-ray variations being much stronger than those at lower energies. The observed lack of spectral variability in the X-rays and similarity between the different wave band light curves argue further against the specific model described above.

However, it should be kept in mind that this argument is valid only above the spectral break, while for this object the break falls close to the *ROSAT* band. Indeed, *Ginga* observations of PKS 2155−304 show that the spectrum continues smoothly to higher energies, and there is evidence of spectral variability at these higher energies (Sembay et al. 1993).

4.1.2.3. Emission from a Shock Front

As mentioned in § 4.1.2.1, the short ultraviolet/X-ray lag argues for a flattened geometry. As shown by Marscher & Gear (1985), a shock front in a relativistic jet would produce both a flattened geometry and the particle acceleration and magnetic field amplification required to produce synchrotron flares. Such shock waves would presumably be caused by the nonstationary energy input responsible for the variations.

Since the distance traveled behind the shock front by a relativistic electron before suffering radiative losses would depend on energy, the thickness of the emission region would decrease with increasing frequency. This would naturally produce the X-ray/ultraviolet lag, and account for its being shorter than the variability timescales. Furthermore, simulated light curves published by Marscher, Gear, & Travis (1992) bear some qualitative resemblance to the observed light curves, with similar shapes at high frequencies and a small but significant time delay toward lower frequencies, although this is difficult to quantify. Finally, the radio data show a spectral flattening throughout the flux rise, which is qualitatively consistent with the Compton loss stage of the shock (Marscher & Gear 1985). However, shock fronts alone cannot solve all the problems with the relativistic jet model, since spectral variability would still inevitably be expected, and invoking a shock front introduces even more free parameters for these already poorly constrained data.

4.2. *The Accretion Disk Model*

Wandel & Urry (1991) proposed that the ultraviolet continuum of PKS 2155−304 could be thermal emission from an accretion disk. There is evidence that emission from an accretion flow contributes to the ultraviolet spectra of Seyfert 1 galaxies. This includes the success of disk models in reproducing their spectra (e.g., Malkan & Sargent 1982) and the observed anticorrelation between the degree of variability and luminosity (e.g., Edelson et al. 1990).

However, the observation that BL Lac objects as a group show a positive correlation between luminosity and variability amplitude (Edelson 1992), poses severe problems for the model of thermal ultraviolet emission from BL Lac objects Also, the linear polarization of PKS 2155−304 has been observed to increase toward shorter wavelengths in previous optical observations (Smith & Sitko 1991), this campaign (Smith et al. 1992; Paper III), and ultraviolet observations with the *Hubble Space Telescope* (Allen et al. 1993). Emission from an accretion disk would be expected to show the opposite behavior.

The current study found that the entire SED of PKS 2155−304 rose and fell with very nearly constant spectral shape. This result is difficult to reconcile with the accretion disk model, for two additional reasons. First, one would expect a measurable *lag* between the ultraviolet and optical bands, because the higher energy emission would be produced at smaller radii. In the model of Wandel & Urry (1991), the 1400 Å flux is produced at radius of $\sim 2 \times 10^{15}$ cm (20 lt-hr), while the 5000 Å flux comes from a distance of $\sim 7 \times 10^{15}$ cm (70 lt-hr). However, the 1400–5000 Å correlation analyses show no evidence for a lag, with an upper limit of a few hours. Thus, the accretion disk model would require the disturbance to propagate at $\gg 10c$. This discrepancy is too large to be accounted for by relatively minor effects such as possible nonaxisymmetry and inhomogeneities in the disk. While monitoring of the Seyfert galaxy NGC 5548 has also failed to measure a 1400–2800 Å lag, that experiment had much lower temporal resolution (4 days), and the propagation speed was limited to only $\gtrsim 0.1c$.

Second, one would expect the *shape* of the infrared through ultraviolet SED to vary with time, since the ultraviolet emission would be dominated by the accretion disk, while another component (presumably with different variability behavior) would have to produce the optical/infrared emission. Such a predicted hardening of the optical/ultraviolet SED as the flux level increases has been observed in Seyfert 1 galaxies and quasars (Cutri et al. 1985; Edelson et al. 1990). However, as mentioned earlier, the shape of the SED of PKS 2155−304 remained very stable as the flux varied, with multiwavelength flux ratios such as F_{1400}/F_{5000} remaining fixed at $\sim 10\%$ while the overall flux level changed by a factor of 2. This argues that the optical/ultraviolet SED is a single emission component, not the combination of components called for in the accretion disk model. These disagreements, when combined with the earlier ones, effectively rule out the accretion disk model.

4.3. *Gravitational Microlensing*

The gravitational microlensing model can also produce the approximately achromatic behavior that was observed in PKS 2155−304. In this picture, the observed variations could be caused by the relative motion of the background quasar and a foreground star cluster (Stickel, Fried, & Kühr 1988; Schneider & Weiss 1987). (If one assumes that the variability is intrinsic to the background source, such as an optically violently variable quasar [Ostriker & Vietri 1985, 1990], then one must still explain its variability.) It requires that a foreground galaxy be closely aligned with PKS 2155−304, so that the line of sight intersects a large number of densely packed stars. Rapid, apparently stochastic variations could than be possible (e.g., Kayser et al. 1989), provided that the background source moves rapidly with respect to the foreground lens (as would be the case of an aligned relativistic jet). If the size of the emission volume is independent of wavelength, then the variability timescales would also be independent of wavelength.

The result that the X-rays lead the ultraviolet by 2–3 hr can be understood if the X-rays arise in a smaller region. Then one would expect that the ultraviolet light curve should be smoother than the X-ray light curve (because the lensing star will have a longer crossing time and possibly weaker amplification). This means that the autocorrelation function of the ultraviolet light curve would be wider than the X-ray autocorrelation function. Unfortunately, given the gaps and the short length of the data train, as well as the differences in the sampling patterns, the ultraviolet and X-ray light curves cannot be used to test this prediction quantitatively.

Another problem for PKS 2155−304 in particlar is that it is the brightest AGN in the far-ultraviolet ($\lesssim$100 eV) sky (Pounds et al. 1991). The interstellar medium of the lensing galaxy might be expected to strongly attenuate the observed far-ultraviolet continuum, even if the lensing galaxy is at a redshift of $z \sim 0.1$ (Falomo et al. 1991). However, this may not be a problem if the lensing galaxy was an elliptical.

5. CONCLUSIONS

This paper reports the results of the first multiwavelength BL Lac objects monitoring campaign for which the data quality, sampling, and total duration were sufficient to measure temporal correlations and lags between X-ray, ultraviolet, and optical wave bands. Three days of intensive observations (once every 96 minutes) were made at X-ray, ultraviolet, and optical wavelengths, and a month of longer wavelength monitoring was made at lower temporal resolution (about once a day).

Four methods for measuring the correlation and lags between light curves were systematically compared. The DCF provides the only method that is formally sensitive to the strength of the correlation. The χ^2 method yielded the most strongly constrained estimate of the lag.

The observational results are the following:

1. The most important result is that variations in the optical, ultraviolet, and X-ray bands were seen to be strongly correlated, with the X-ray variations leading the lower wavelengths by a statistically significant amount (2–3 hr). No measurable lag was found between the optical and ultraviolet bands, down to a limit of $\sim$2 hr.

2. The optical/ultraviolet light curves showed a factor of $\sim$2 variation in a week, and the optical/ultraviolet/X-ray light curves showed $\sim$10% changes on timescales as short as a few hours. These doubling timescales are much longer than the lags and upper limits measured between wave bands.

3. The amplitudes of the variations were independent of wavelength in the infrared through X-ray range. The spectral index and overall shape of the SED remained fixed (with multiband flux ratios constant to within 10%) as the overall flux varied by a factor of 2.

4. The sampling was worse at longer wavelengths, and the infrared appears to be correlated with the optical/ultraviolet, but no lag could be reliably measured. The amplitude of the radio variations became progressively weaker to longer wavelengths, and the sampling was even worse than the infrared, although the data are suggestive of a correlation, with variations occurring $\sim$1 week after the optical/ultraviolet.

5. None of the light curves showed any statistically significant evidence of periodic variations or the QPO behavior seen in compact binaries.

These results have important implications for models of the broadband emission. The accretion disk model (Wandel & Urry 1991), which has been criticized on other grounds (Smith & Sitko 1991; Edelson 1992), is now even more strongly ruled out. It would predict a measurable lag between ultraviolet and optical wave bands and that the shape of the ultraviolet/optical SED should vary with flux. Neither of these effects was observed.

The results of the multiwavelength monitoring also argue against the soft X-rays being produced by the Compton process. They cannot be produced by self-Compton upscattering of synchrotron photons from a homogeneous region, because the soft X-rays *lead* the lower frequency emission. It is also difficult to produce the X-rays by Compton upscattering of independent seed photons, without producing a flatter ultraviolet/X-ray SED than observed.

The gravitational microlensing model (Ostriker & Vietri 1985, 1990) predicts that, given the X-ray/ultraviolet lag, the X-rays should vary somewhat more rapidly than the ultraviolet, but these data are not sufficiently well sampled to test this. One might also expect that the X-rays should be attenuated by the lensing galaxy, unless it was an elliptical, but, again, there is no firm information on the nature of the putative lensing galaxy. Thus, these data do not allow a clear test of the microlensing model.

The strong X-ray/ultraviolet correlation, combined with the fact that the X-rays lead the ultraviolet, may be more consistent with the entire radio through soft X-ray SED arising from direct synchrotron emission from a relativistic jet. This would require the electron distribution to extend to higher energies than necessary to produce only the radio through ultraviolet SED.

In the tapered jet model (Ghisellini et al. 1985), the electron density and magnetic field strength vary smoothly along the jet. The most natural explanation of the lag is then that the X-rays are generated closest to the site of electron acceleration and the ultraviolet comes from farther out. However, this would then predict strong spectral variability (which is not observed) and a larger X-ray/ultraviolet lag than was observed. Further modeling will be needed to see whether relativistic corrections and other effects can account for these discrepancies.

The observation that the X-rays lead the ultraviolet/optical by much less than the variability timescale argues for a flattened geometry, such as might be expected at a shock front in

the jet. While this may seem like the most attractive remaining possibility, it is still difficult to reconcile the similarity of the X-ray and ultraviolet light curves (with no strong spectral variability within or between any band) and the short lifetimes predicted by most jet models for the X-ray–emitting electrons.

The authors would like to thank W. H. Press for his assistance with understanding the χ^2 method. This work was supported in part by NASA grant NAG 5-1034. A. P. M. was supported in part by NSF grant AST 91-16525 and NASA grant NAGW-1608. A. V. F. acknowledges the support of NSF grant AST 89-57063. M. L. S. acknowledges the support of the University Research Council of the University of Cincinnati. K. H. acknowledges support from NASA grant NAGW-2678. E. D. F. and R. I. K. acknowledge the support of NASA grant NAGW-2120.

REFERENCES

Allen, R. G., Smith, P. S., Angel, J. R. P., Miller, B. W., Anderson, S. F., & Margon, B. 1993, ApJ, 403, 610
Blandford, R., & Rees, M. J. 1978, in Pittsburgh Conference on BL Lac objects, ed. A. M. Wolfe (Pittsburgh: Univ. Pittsburgh Press), 328
Bracewell, R. N. 1986, The Fourier Transform and Its Applications (2d ed.; New York: McGraw-Hill)
Bregman, J. 1990, Astron. Astrophys. Rev., 2, 125
Brinkmann, W., et al. 1994, A&A, 288, 433 (Paper II)
Celotti, A., Maraschi, L., & Treves, A. 1991, ApJ, 337, 403
Clavel, J., et al. 1991, ApJ, 366, 64
Cohen, M., & Unwin, S. 1981, in IAU Symp. 97, Extragalactic Radio Sources, ed. D. Heeschen & C. Wade (Dordrecht: Reidel), 345
Courvoisier, T., et al. 1995, ApJ, 438, 108 (Paper III)
Cutri, R., Wiśniewski, W. Z., Rieke, G. H., & Lebofsky, M. J. 1985, ApJ, 296, 423
Daves, S. 1990, MNRAS, 244, 93
Done, C., Madejski, G. W., Mushotzky, R. F., Turner, T. J., Koyama, K., & Kunieda, H. 1992, ApJ, 400, 138
Edelson, R. 1992, ApJ, 410, 516
Edelson, R., & Krolik, J. H. 1988, ApJ, 333, 646
Edelson, R., Krolik, J., & Pike, G. 1990, ApJ, 359, 86
Edelson, R., et al. 1991, ApJ, 372, L9
Falomo, R., Giraud, E., Maraschi, L., Melnick, J., Tanzi, E. G., & Treves, A. 1991, ApJ, 380, L67
George, I., Warwick, R., & Bromage, G. 1988, in A Decade of UV Astronomy with *IUE*, ed. Y. Kondo (Paris: ESA), 2, 287
Ghisellini, G., & Maraschi, L. 1989, ApJ, 340, 181
Ghisellini, G., Maraschi, L., & Treves, A. 1985, A&A, 146, 204
Horne, K., Welsh, W., & Peterson, B. 1991, ApJ, 367, L5
Hufnagel, B., & Bregman, J. 1992, ApJ, 386, 473
Kayser, R., Weiss, A., Refsdal, S., & Schreider, P. 1989, A&A, 214, 4
Königl, A. 1989, in BL Lac Objects, ed. L. Maraschi, T. Maccacaro, & M. H. Ulrich (Berlin: Springer-Verlag), 281
Krolik, J. H., Horne, K., Kallman, T. R., Malkan, M. A., Edelson, R. A., & Kriss, G. A. 1991, ApJ, 371, 541
Leighly, K., Kunieda, H., Tsusaka, Y., Awaki, H., & Tsuruta, S. 1994, ApJ, 421, 69
Malkan, M. A., & Sargent, W. L. W. 1982, ApJ, 254, 22
Mandelbrot, B. B. 1969, Water Resources Res., 5, 228
Maraschi, L. 1992, in Variability of Blazars, ed. E. Valtaoja & M. Valtonen (Cambridge: Cambridge Univ. Press), 447
Maraschi, L., Ghisellini, G., & Celotti, A. 1992, ApJ, 395, L5
Marscher, A. P. 1980, ApJ, 235, 386
Marscher, A. P., & Gear, W. K. 1985, ApJ, 298, 114
Marscher, A. P., Gear, W. K., & Travis, J. P. 1992, in Variability of Blazars, ed. E. Valtaoja & M. Valtonen (Cambridge: Cambridge Univ. Press), 85
Marscher, A. P., Marshall, F. E., Mushotzky, R. F., Dent, W. A., Balonek, T. J., & Hartman, R. F. 1979, ApJ, 233, 498
Melia, F., & Königl, A. 1989, ApJ, 340, 162
Mittaz, J., & Branduardi-Raymont, G. 1989, MNRAS, 328, 1029
Mufson, S. L., Hutter, D. J., Kondo, Y., Urry, C-M., & Wiśniewski, W. Z. 1990, ApJ, 354, 116
Ostriker, J. P., & Vietri, M. 1985, Nature, 318, 446
———. 1990, Nature, 344, 45
Pounds, K., et al. 1991, MNRAS, 253, 364
Press, W. 1978, Comm. Astrophys., 7, 103
Press, W., Rybicki, G., & Hewitt, J. 1992, ApJ, 385, 404
Quirrenbach, A., et al. 1991, ApJ, 372, L71
Schneider, P., & Weiss, A. 1987, A&A, 171, 49
Sembay, S., Warwick, R. S., Urry, C. M., Sokoloski, J., George, I. M., Makino, F., Ohashi, T., & Tashiro, M. 1993, ApJ, 404, 112
Smith, P. S., Hall, P. B., Allen, R. G., & Sitko, M. L. 1992, ApJ, 400, 115
Smith, P. S., & Sitko, M. 1991, ApJ, 383, 580
Stickel, M., Fried, J. W., & Kühr, H. 1988, A&A, 191, L16
Tagliaferri, G., Stella, L., Maraschi, L., Treves, A., & Celotti, A. 1991, ApJ, 380, 78
Treves, A., et al. 1989, ApJ, 341, 733
Urry, C. M., et al. 1993, ApJ, 411, 614 (Paper I)
Urry, C. M., & Mushotzky, R. 1982, ApJ, 253, 38
van der Klis, 1989, ARA&A, 27, 517
Walter, R., & Courvoisier, T. J.-L. 1991, A&A, 250, 312
Wandel, A., & Urry, C. M. 1991, ApJ, 367, 78